US
UNIVERSITY OF SUSSEX

Sussex Research

From the cell membrane to the nucleus: unearthing transport mechanisms for Dynein

Laurie Crossley, Caroline A Garrett, Majid Hafezparast, Anotida Madzvamuse

Publication date
01-09-2012

Licence
This work is made available under the Copyright not evaluated licence and should only be used in accordance with that licence. For more information on the specific terms, consult the repository record for this item.

Citation for this work (American Psychological Association 7th edition)
Crossley, L., Garrett, C. A., Hafezparast, M., & Madzvamuse, A. (2012). *From the cell membrane to the nucleus: unearthing transport mechanisms for Dynein* (Version 1). University of Sussex. https://hdl.handle.net/10779/uos.23387153.v1

Published in
Bulletin of Mathematical Biology

Link to external publisher version
https://doi.org/10.1007/s11538-012-9745-x

Copyright and reuse:
This work was downloaded from Sussex Research Open (SRO). This document is made available in line with publisher policy and may differ from the published version. Please cite the published version where possible. Copyright and all moral rights to the version of the paper presented here belong to the individual author(s) and/or other copyright owners unless otherwise stated. For more information on this work, SRO or to report an issue, you can contact the repository administrators at sro@sussex.ac.uk. Discover more of the University's research at https://sussex.figshare.com/

From the Cell Membrane to the Nucleus: Unearthing Transport Mechanisms for Dynein

Laurie Crossley[*], Caroline A. Garrett[†], Majid Hafezparast[†], and Anotida Madzvamuse[‡]

April 18, 2012

Abstract

Mutations in the motor protein cytoplasmic dynein have been found to cause Charcot-Marie-Tooth disease in humans, spinal muscular atrophy and severe intellectual disabilities in humans. In mouse models neurodegeneration is observed. We sought to develop a novel model which could incorporate the effect of mutations on distance travelled and velocity. A mechanical model for the dynein mediated transport of endosomes is derived from first principles and solved numerically. The effects of variations in model parameter values are analysed to find those that have a significant impact on velocity and distance travelled. The model successfully describes the processivity of dynein and matches qualitatively the velocity profiles observed in experiments.

Key words

Dynein, Endocytosis, Motor Proteins, Transport Model.

[*]Department of Mathematics, Pev III, 5C15, University of Sussex, Brighton, BN1 9QH, UK
[†]School of Life Sciences, John Maynard Smith Building, University of Sussex, Brighton, BN1 9QG, UK
[‡]Corresponding author: a.madzvamuse@sussex.ac.uk

1 Introduction

The endocytic pathway is a subject at the forefront of current research although the specific details of the process are yet to be fully discovered. In mammalian cells, Epidermal Growth Factor (EGF) receptors activated by EGF are transported from the cell membrane to the perinucleur region to be degraded or recycled back to the cell membrane, in a process known as endocytosis (see Figure 1). Activated EGF receptors are transported in clathrin-coated vesicles which undergo fusion to form early endosomes. Receptors to be degraded will then be transported in late endosomes which fuse with lysosomes [16, 38, 40]. Endosomes are bidirectional and experience fusion and fission along the endocytic pathway [38]. This transport process involves the action of motor proteins which attach to the vesicles or endosomes and move along microtubules or actin filaments, which form the cytoskeleton. Microtubules are polarised, with the plus-end usually pointing towards the cell membrane, away from the nucleus [40]. There are numerous articles providing supporting evidence as to which motor proteins are involved in each stage of the process, although they do not always agree [3, 5, 12, 23, 33]. These differences may be due to the differences in results from the studies of different types of cells, experimental techniques and differences between in vitro and in vivo studies.

In this study, we are concerned with the involvement of the motor protein cytoplasmic dynein. Dynein is a processive motor which moves towards the minus-end of the microtubule towards the nucleus. The motor domain, also referred to as the dynein "head", has a hexameric ring of adenosine triphosphatases (ATPases) associated with diverse cellular activity (AAA+). Of these four bind ATP and are responsible for producing the energy through ATP hydrolysis for dynein motility [7, 28, 50]. There is a stalk comprising of a coiled coil, which extends from the AAA+ ring and ends with a globular microtubule-binding domain (MTBD) [7, 28, 50]. There is also a newly identified feature labelled a *strut* or *buttress* which, it is proposed, supports the stalk under load [7, 28]. At the opposite terminus to the head is the tail structure which is associated with intermediate, light intermediate and light chains (from the Tctex1/rp3, roadblock and LC8 families). Regulators such as the dynactin complex also bind the tail region [50]. The movement of cytoplasmic dynein is powered by ATP hydrolysis. Binding of ATP to the head results in the dissociation of MTBD from microtubules and a shift in the linker position (which connects the dynein head and tail), so that instead of spanning the hexameric face where it contacts AAA1 and AAA4, it moves to contact AAA2, a movement of around 17 nm. The MTBD progresses along the microtubules and as the

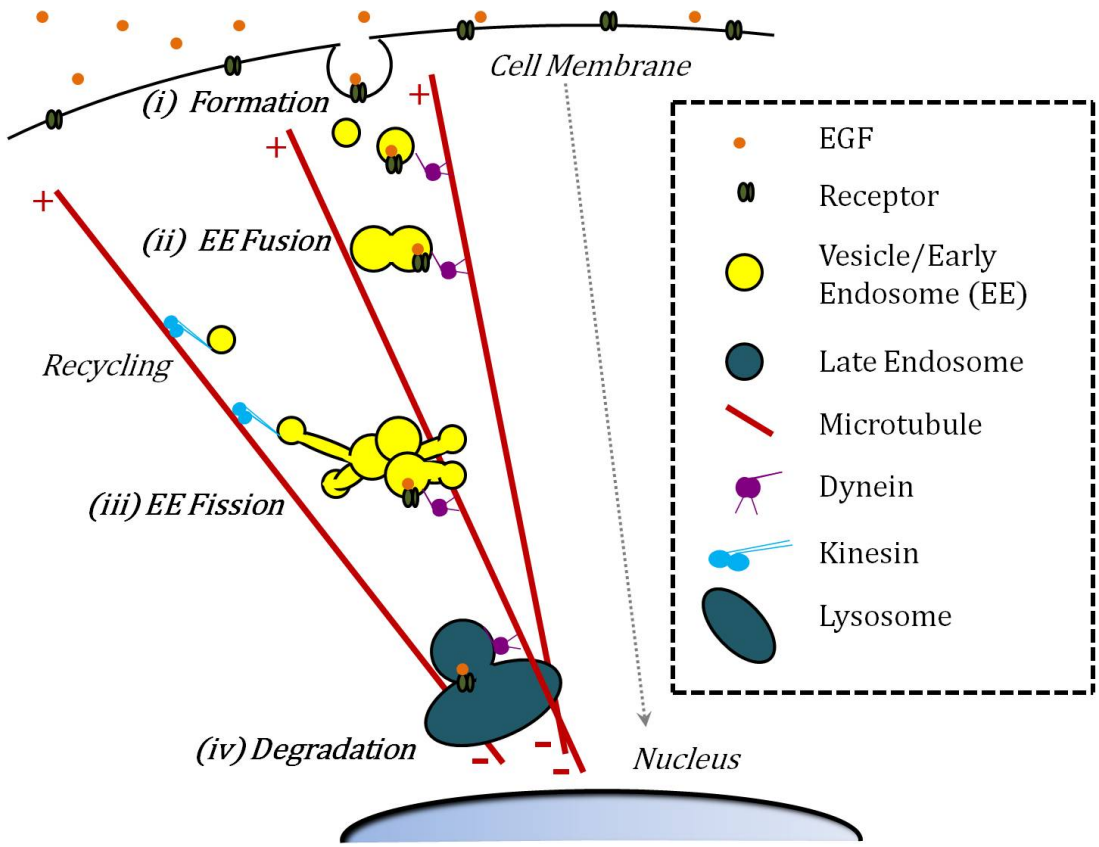

Figure 1: (Colour version online) From the cell membrane to the nucleus: A schematic diagram of the clathrin-mediated endocytic pathway for EGF receptors. (i) Activated EGF receptors and the surrounding membrane invaginates whilst a clathrin coat forms around it. (ii) The clathrin coat dissembles and the receptors are transported along microtubules in vesicles, which undergo fusion to form early endosomes. (iii) Endosomes undergo fission, resulting in the separation of the contents destined for degradation and that to be recycled back to the cell membrane. (iv) Activated receptors to be degraded will then be transported in late endosomes which fuse with lysosomes. The transport process involves the action of motor proteins which attach to the vesicles or endosomes and move along microtubules.

products of ATP hydrolysis; adenosine diphosphate (ADP) + Pi are released the MTBD once again forms a strong association with microtubules and the linker moves back to its original position thus producing the power stroke of dynein [26, 28, 38, 41, 44]. The motor domains of dynein coordinate so that it appears to "walk" along the microtubule. The step size is usually 8 nm, although it has also been found to take the values of 16, 24 and 32 nm [36, 40]. Mutations in the tail region of the cytoplasmic dynein causing Charcot-Marie-Tooth disease, intellectual disability [52] and spinal muscular dystrophy [20] in humans and neurodegeneration in mouse models have been described [8, 14, 19, 51]. These mutations are likely to compromise the structure and the assembly of cytoplasmic dynein complex. Since dynein movement along the microtubules is a coordinated process between the two motors and their tail domains, such mutations could therefore impact

their affinities to the cargo or microtubules and subsequently impair their functions. We therefore wish to derive a mathematical model for the transport mechanism of dynein from first principles. This model could be used to predict how mutations might affect the transport process with relation to the distances travelled and the velocity profiles.

Next we outline how this article is structured. In Section 2, we detail how experimental data on the transport process was gathered. We then derive the mathematical model from first principles in Section 3. We proceed to solve the model system numerically in Section 5, demonstrating the lack of steady states of the model and the effects of variations in parameters. The model describes the processivity of cytoplasmic dynein as there are no steady states. The velocity profiles of the model qualitatively matches those observed experimentally. We also found that the most significant parameters of the model, that will affect greatly the velocity and distance travelled, are the force produced by the AAA+ ring, the unstressed spring length representing the tail structure, and the spring constant representing the stalk (see Figure 4).

2 Experiments

Mouse embryonic fibroblasts (MEFs) were cultured in Lab-Tek II chamber slides to 40% confluency in culture medium; Dulbeccos Modified Eagles Medium (DMEM) supplemented with 15% Hyclone, 1% Penicillin/Streptomycin and 1% L-Glutamine. Cells were cultured in a 37 ℃ incubator with 3% O_2 and 5% CO_2. The MEFs were then starved for 2 hrs in the culture medium without Hyclone, before the addition of 20 ng/ml EGF - Alexa Fluor 555 (Invitrogen). Cells were incubated for 10 mins at 37 ℃ before being rinsed and left in warmed Leibovitzs L-15 CO_2 independent media (Gibco) for imaging. Images were collected at 5 min intervals post removal of EGF and up to a maximum of 30 mins. For each time point images were captured every 2 secs for 1 min (a 0.2 sec exposure time at 100% transmission was used for image collect via a TRITC filter). A personal Delta Vision (pDV) microscope from Applied Precision was used for image acquisition (see Figure 2).

The experimental data was analysed using the image processing program ImageJ to facilitate the manual tracking of endosomes via the Manual Tracking plugin by Fabrice Cordelierés [9]. ImageJ outputs data on the distance travelled and velocity of the endosomes for each slice of an image sequence. Four visibly fast, retrograde moving endosomes from each cell were tracked and an

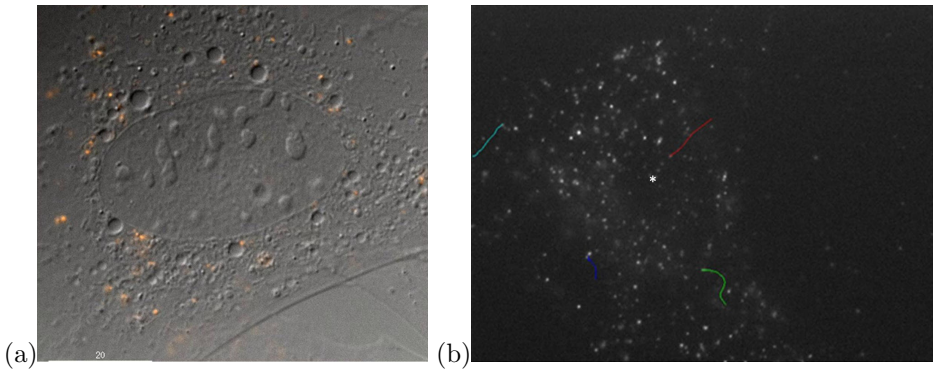

Figure 2: (Colour version online) Live-cell tracking of Epidermal Growth Factor (EGF). MEFs were starved for 2 hours and subsequently stimulated for 10 mins with 20ng/ml EGF - Alexa Fluor 555. EGF was removed and Live cell images captured on a personal Delta Vision up to 30 min post removal of EGF. (a) EGF movement was manually tracked using Image J [9]. (b) Typical wild-type trajectories captured at the 30 min time point and tracked using Image J. * indicates the location of the nucleus.

average speed per second and total distance moved was calculated for each endosome (see Figure 2). The start of a track was determined when the endosome moved at a speed greater than 0.2 microns per second and stopped when either the end of frame sequences was reached or the endosome moved out of focus, or the endosomes speed decreased to less than 0.2 microns per second and did not increase in speed again. This data is useful to analyse the movement of endosomes. However, it must be noted that ImageJ has intrinsic limitations. For example, any human error in tracking an endosome will be significant due to the small distances involved. Endosomes can disappear as they travel through the cell, they can also fuse and separate thereby causing problems in tracking over the whole time period. The results are also restricted by the limitations of a two-dimensional image sequence capturing a three dimensional process. These limitations provide further motivation to derive a mathematical model in order to obtain an accurate representation which can be used to compare and validate experimental data as well as to make hypothetical predictions testable in laboratories. Using data obtained from in-vitro assays and through the use of ImageJ, we plot a sample of velocities of individually tracked endosomes as shown in Figure 3.

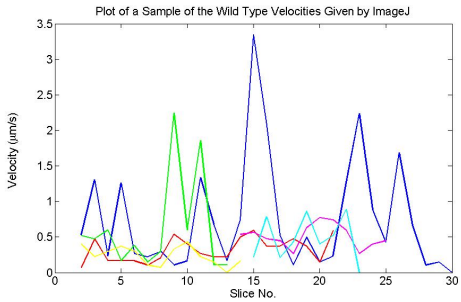

Figure 3: (Colour version online) Plot of a sample of velocities from the individually tracked EGF movements in wild type cells using ImageJ [9]; each tracked EGF movement is represented in a different colour. Live cell images were captured on a personal Delta Vision, at 2 sec intervals, 30 min post removal of EGF. A slice number of N represents the Nth image captured at a time of $2N$ sec. The plot shows that the velocities have an oscillatory profile over time.

3 Derivation of the Mathematical Model

3.1 Overview of Current Mathematical Models

Several papers have been written on modelling endocytosis and the distribution and motion of kinesins, another motor protein family; however, to the authors' knowledge, relatively few have been formulated to describe the transport process of dynein. Smith and Simmons [47] model the motor-assited transport of cell organelles and vesicles by a reaction-diffusion-transport equation and other authors have extended this model [11, 15, 31, 32, 54]. Ashwin *et al.,* [2] use an asymmetric simple exclusion process to model the motion of dynein along microtubles, both dynein that is carried towards the positive-end by kinesin and dynein that moves towards the negative-end. Schuster *et al.,* [45] extended this model to study the loading of endosomes onto dynein. Other authors model multiple motor based transport [13, 29, 30]. A paper by Mukherji [36] proposes a model for dynein by considering its mechanochemical cycle. The model assumes that dynein has a single head and focuses on the time evolution with respect to ATP hydrolysis at the binding sites. Another paper by Tsygankov *et al.,* [49] models the coordinated stepping of dynein also by considering the mechanochemical cycle.

Several authors have modelled the processive stepping mechanism of kinesin [4, 22, 25, 37, 55, 56] using a power stroke phase followed by a random diffusional search for the next binding point. Munárriz *et al.,* [37] use a simple flashing ratchet model. Zhang develops an earlier Brownian stepper model by Bier, and later develops a two-cycle mechanochemical network model [55, 56].

Imafuku *et al.,* [25] extend the stepping model to incorporate the tendency of kinesin to hop backwards. Bier and Cao [4] also propose a model to include these backsteps and find that they can speed up a processive motor protein. Hendricks *et al.,* [22] also model the stepping process of kinesin by a mechanistic model. The model involves the weakly bound rearward head of the kinesin motor protein being propelled forward by a conformational change whilst the front head is strongly bound. The rearward head then undergoes Brownian motion to reach the next unoccupied binding site. The two heads are assumed to connect to a neck by a linker, which is modelled as a spring, and the neck is also connected to the cargo by a linker, again modelled as a spring. We use a similar mechanical approach with regards to the dynein structure in order to derive a mathematical model from first principles for the transport mechanism of dynein.

3.2 Derivation of the Mechanical Model from First Principles

To date, very little work has been done on mathematical modelling of the mechanisms describing the transport process for dynein from the cell membrane to the nucleus. To the best of our knowledge, this study is the first to derive, from first principles, a mathematical model to understand transport mechanisms for dynein. We propose a mechanical model for the motion of a single dynein pulling an endosome. We model the endosome, AAA+ rings of the dynein motor domain and dynein microtubule-binding domains (MTBDs) as spheres, as shown in Figure 4. We refer to the endosome as the cargo. We also model the stalks of the dynein as springs. The tail structure of the dynein is modelled as two separate springs each connecting an AAA+ ring to the binding point on the cargo. Taking the microtubule to be a one-dimensional line with the positive direction towards the nucleus, we therefore consider movement only on the microtubule. For simplicity, we only consider horizontal forces. Let us denote by x_C, x_A, x_B, x_D and x_E the positions of the cargo, AAA+ rings labelled A and B, and MTBDs labelled D and E respectively, all with respect to time t (see Figure 4). We assume that each AAA+ ring produces a horizontal force towards the minus-end of the microtubule, F_A and F_B for the respective AAA+ ring, which is dependent on the respective positions of MTBDs D and E. We define F_C to be a constant force acting on the cargo in the negative direction. We assume that there exist forces, the binding affinity, between the microtubule and the MTBD, defined as f and g for MTBDs D and E respectively, which depend on the MTBD's repective positions.

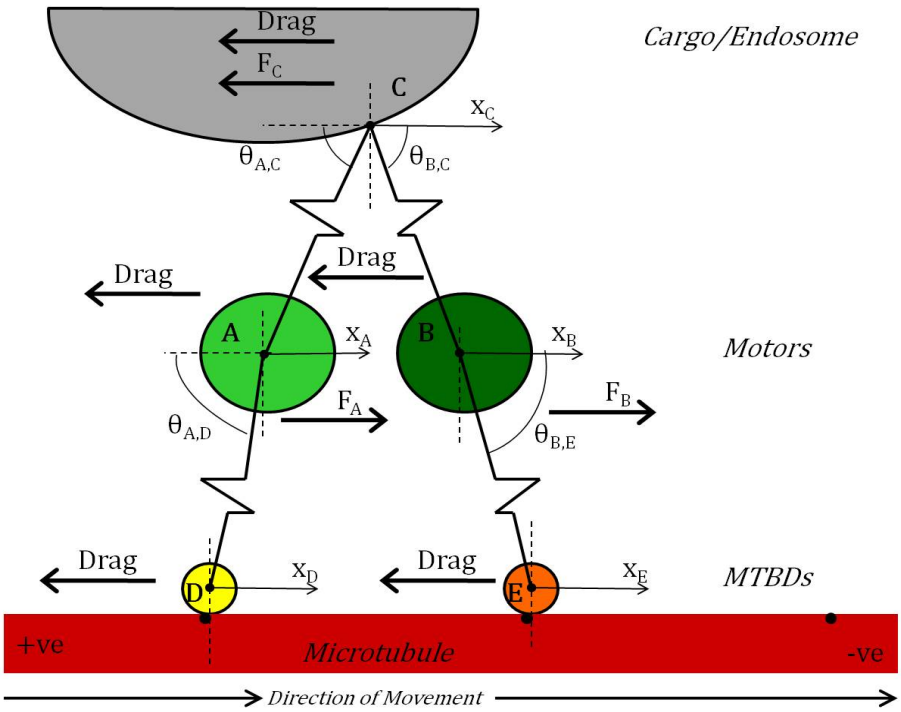

Figure 4: (Colour version online) Schematic diagram of the mechanical model. The cargo is modelled as a sphere and depicted in grey. The dynein motor domain is modelled by two spheres, representing the AAA+ rings (depicted in green), connected via springs, representing the stalks, to two smaller spheres, representing the MTBDs D and E (depicted in yellow and orange respectively). The tail section of dynein is modelled as two springs connecting the AAA+ rings to the cargo. The microtubule is modelled as a line and depicted in red.

We calculate the spring forces using Hooke's Law stated as:

$$F_1 = K(x - l), \tag{1}$$

where F_1 is the force exerted by the spring, l is the unstressed length of the spring, x is the length of the spring and K is the associated spring constant. If we have a force at an angle that is neither horizontal nor vertical, we need to break this force down into its horizontal and vertical components. Since we only consider the horizontal forces we only use the trigonometric result:

$$F_2 = Y \cos\theta, \tag{2}$$

where F_2 is the resultant horizontal force and Y is the force given at an angle θ to the horizontal. The cargo, AAA+ rings and stalks will all experience viscous drag. If we assume that these all

have very small Reynold's numbers and are spherical then by Stokes' Law:

$$F_3 = -6\pi\mu R v, \tag{3}$$

where F_3 is the frictional force, μ the dynamic viscosity, R the radius of the sphere and v the settling velocity. Denote by m_C, m_A, m_B, m_D and m_E the masses of the cargo, AAA+ rings labelled A and B, and MTBDs labelled D and E respectively. Newton's second law states that, if we assume that the masses are constant, the mass multiplied by the acceleration must equal the balance of the forces. Using this law we derive the following system of second order non-linear ordinary differential equations (ODEs):

$$\begin{aligned}
m_C\frac{d^2x_C}{dt^2} =& K_{B,C}\Big[x_B - x_C - L_{B,C}\cos[\theta_{B,C}(x_A, x_B, x_C)]\Big] \\
&- K_{A,C}\Big[x_C - x_A - L_{A,C}\cos[\theta_{A,C}(x_A, x_B, x_C)]\Big] - F_C - \gamma_C\frac{dx_C}{dt}, && (4)\\
m_A\frac{d^2x_A}{dt^2} =& F_A(x_D, x_E) + K_{A,C}\Big[x_C - x_A - L_{A,C}\cos[\theta_{A,C}(x_A, x_B, x_C)]\Big] \\
&- K_{A,D}\Big[x_A - x_D - L_{A,D}\cos[\theta_{A,D}(x_A, x_B)]] - \gamma_A\frac{dx_A}{dt}, && (5)\\
m_B\frac{d^2x_B}{dt^2} =& F_B(x_D, x_E) + K_{B,E}\Big[x_E - x_B - L_{B,E}\cos[\theta_{B,E}(x_A, x_B)]\Big] \\
&- K_{B,C}\Big[x_B - x_C - L_{B,C}\cos[\theta_{B,C}(x_A, x_B, x_C)]\Big] - \gamma_B\frac{dx_B}{dt}, && (6)\\
m_D\frac{d^2x_D}{dt^2} =& f(x_D, x_E) + K_{A,D}\Big[x_A - x_D - L_{A,D}\cos[\theta_{A,D}(x_A, x_B)]\Big] - \gamma_D\frac{dx_D}{dt}, && (7)\\
m_E\frac{d^2x_E}{dt^2} =& g(x_D, x_E) - K_{B,E}\Big[x_E - x_B - L_{B,E}\cos[\theta_{B,E}(x_A, x_B)]\Big] - \gamma_E\frac{dx_E}{dt}, && (8)
\end{aligned}$$

where $\frac{d^2x_i}{dt^2}$ denotes the acceleration and $\frac{dx_i}{dt}$ represents the velocity ($i = A$, B, etc). Note that we denote by B, C the connection between B and C and similarly for other connections.

First, we present the derivation of the equation describing how the cargo x_C is transported. In the equation of motion for x_C we have mass multiplied by acceleration on the left hand side whilst on the right hand side we balance the forces acting on the cargo. There are two spring forces acting on the cargo. First we look at the spring force between the cargo and the AAA+ ring B, we denote this force by $F_{B,C}$. By combining (1) and (2) we have:

$$F_{B,C} = K_{B,C}\Big[\frac{x_B - x_C}{\cos[\theta_{B,C}(x_A, x_B, x_C)]} - L_{B,C}\Big]\cos[\theta_{B,C}(x_A, x_B, x_C)],$$

where $K_{B,C}$ is the spring constant associated with the spring, $L_{B,C}$ is the unstressed length of the

spring, $\theta_{B,C}(x_A, x_B, x_C)$ is the acute angle of the spring from the horizontal and

$$\frac{x_B - x_C}{\cos[\theta_{B,C}(x_A, x_B, x_C)]}$$

is the length of the spring at time t. The above simplifies to:

$$F_{B,C} = K_{B,C}\Big[x_B - x_C - L_{B,C}\cos[\theta_{B,C}(x_A, x_B, x_C)]\Big].$$

Equivalently, the spring force between the cargo and the AAA+ ring A, denoted here by $F_{A,C}$, is given by:

$$F_{A,C} = -K_{A,C}\Big[x_C - x_A - L_{A,C}\cos[\theta_{A,C}(x_A, x_B, x_C)]\Big],$$

where $K_{A,C}$ is the spring constant, $L_{A,C}$ is the unstressed spring length and $\theta_{A,C}(x_A, x_B, x_C)$ is the acute angle of the spring from the horizontal. This force is negative as it acts in the opposite direction to positive x_C. Another force that acts on the cargo is F_C which is a constant force applied in the negative x_C direction. We consider this force to be fixed and constant. The final force that we need to consider is the viscous drag, denoted by D_C. If we assume that the cargo satisfies the conditions of Stokes' Law then by (3) we have:

$$D_C = -\gamma_C \frac{dx_C}{dt},$$

where γ_C is the damping coefficient, that is $\gamma_C = 6\pi\mu R_C$ with μ the viscosity of the cytoplasm and R_C the radius of the cargo. The force is negative as it acts in the opposite direction to x_C. We can now sum the forces to obtain the right hand side of (4). This completes the derivation of the equation describing how the cargo is transported.

In a similar fashion, we derive the equation of motion for the AAA+ ring A (5). Assume that the AAA+ ring A produces a force $F_A(x_D, x_E)$ which depends on the respective positions of MTBDs D and E. The spring force between the AAA+ ring A and the cargo, noting that it will act in the opposite direction, is given by:

$$-F_{A,C} = K_{A,C}\Big[x_C - x_A - L_{A,C}\cos[\theta_{A,C}(x_A, x_B, x_C)]\Big],$$

with parameter descriptions similar to those describing x_C. There will also be a spring force

between AAA+ ring A and the MTBD D, which is denoted by $F_{A,D}$ and is given by

$$F_{A,D} = -K_{A,D}\Big[x_A - x_D - L_{A,D}\cos[\theta_{A,D}(x_A, x_B)]\Big],$$

where $K_{A,D}$ is the spring constant, $L_{A,D}$ is the unstressed spring length and $\theta_{A,D}(x_A, x_B)$ is the acute angle of the spring. This force is negative as it acts in the opposite direction to x_A. Finally considering the viscous drag, denoted by D_A; as with the cargo we have

$$D_A = -\gamma_A \frac{dx_A}{dt},$$

where $\gamma_A = 6\pi\mu R_A$ is the damping coefficient with R_A the radius of the AAA+ ring A.

Similarly we can derive the equation of motion for the AAA+ ring B (6) with parameters $K_{B,E}$, $L_{B,E}$ and $\theta_{B,E}(x_A, x_B)$ the spring constant, unstressed length and acute angle for spring between AAA+ ring B and MTBD E respectively; γ_B the damping coefficient with R_B the radius and $F_B(x_D, x_E)$ the force produced by the AAA+ ring B.

We now balance the forces on the MTBD D to obtain the right hand side of (7). The spring force between MTBD D and AAA+ ring A is given by

$$-F_{A,D} = K_{A,D}\Big[x_A - x_D - L_{A,D}\cos[\theta_{A,D}(x_A, x_B)]\Big],$$

where the parameters are the same as those given above. There will also be a force acting on the MTBD D binding it to the microtubule which will depend on the position of the MTBD with respect to the binding site, assumed here to depend on the position of the other MTBDs. We denote the binding force acting in x_D direction by $f(x_D, x_E)$. The final force acting on MTBD D will be the viscous drag, similarly to the cargo, we have:

$$D_D = -\gamma_D \frac{dx_D}{dt},$$

where $\gamma_D = 6\pi\mu R_D$ is the damping coefficient with R_D the radius of the MTBD D.

The derivation of the equation of motion for MTBD E (8) is similar, with the parameters $g(x_D, x_E)$, the horizontal binding force in the x_E direction, and γ_E, the damping coefficient. We will have $\gamma_E = 6\pi\mu R_E$ with R_E the radius of the MTBD E.

To proceed, we make the following reasonable mathematical assumptions:

- The springs between the AAA+ rings and the cargo are equivalent;

$$\begin{cases} K_{A,C} = K_{B,C} =: K_C, \\ L_{A,C} = L_{B,C} =: L_C. \end{cases} \tag{A1}$$

- The springs between the AAA+ rings and the MTBDs are equivalent;

$$\begin{cases} K_{A,D} = K_{B,E} =: K_S, \\ L_{A,D} = L_{B,E} =: L_S. \end{cases} \tag{A2}$$

- The masses of the AAA+ rings are equal and the masses of the MTBDs are equal;

$$\begin{cases} m_A = m_B =: m_M, \\ m_D = m_E =: m_S. \end{cases} \tag{A3}$$

- The damping coefficients of the AAA+ rings are equal and the damping coefficients of the MTBDs are equal;

$$\begin{cases} \gamma_A = \gamma_B =: \gamma_M, \\ \gamma_D = \gamma_E =: \gamma_S. \end{cases} \tag{A4}$$

- The cargo is allowed to move freely, it is only subjected to the action of a single motor in a viscous medium and undergoes no fusion or fission. Hence, there is no added force such as that from other motors or from an optical trap;

$$F_C = 0. \tag{A5}$$

- The cargo is pulled by the dynein such that its tail section is horizontal;

$$\begin{cases} \theta_{B,C} = 0, \\ \theta_{A,C} = \pi. \end{cases} \tag{A6}$$

- The stalks are at an angle such that:

$$\begin{cases} \cos[\theta_{A,D}(x_A, x_B)] \approx 0, \\ \cos[\theta_{B,E}(x_A, x_B)] \approx 0. \end{cases} \tag{A7}$$

We note that some of the above assumptions will be relaxed in our future studies. The goal here is to derive the simplest model possible.

Using assumptions (A1), (A2), (A5)-(A7) we can reduce equations (4) - (8) to:

$$m_C \frac{d^2 x_C}{dt^2} + \gamma_C \frac{dx_C}{dt} + 2K_C x_C = K_C(x_A + x_B - 2L_C), \tag{9}$$

$$m_A \frac{d^2 x_A}{dt^2} + \gamma_A \frac{dx_A}{dt} + (K_C + K_S)x_A = F_A(x_D, x_E) + K_C x_C + K_S x_D + K_C L_C, \tag{10}$$

$$m_B \frac{d^2 x_B}{dt^2} + \gamma_B \frac{dx_B}{dt} + (K_C + K_S)x_B = F_B(x_D, x_E) + K_C x_C + K_S x_E + K_C L_C, \tag{11}$$

$$m_D \frac{d^2 x_D}{dt^2} + \gamma_D \frac{dx_D}{dt} + K_S x_D = f(x_D, x_E) + K_S x_A, \tag{12}$$

$$m_E \frac{d^2 x_E}{dt^2} + \gamma_E \frac{dx_E}{dt} + K_S x_E = g(x_D, x_E) + K_S x_B. \tag{13}$$

Now summing equations (10) and (11), (12) and (13) respectively and using assumptions (A3) and (A4) results in the following nonlinear system of ODEs:

$$m_C \frac{d^2 x_C}{dt^2} + \gamma_C \frac{dx_C}{dt} + 2K_C x_C = K_C(x_A + x_B - 2L_C), \tag{14}$$

$$\begin{aligned} m_M \frac{d^2(x_A + x_B)}{dt^2} &+ \gamma_M \frac{d(x_A + x_B)}{dt} + (K_C + K_S)(x_A + x_B) \\ &= F_A(x_D, x_E) + F_B(x_D, x_E) + 2K_C x_C + K_S(x_D + x_E) + 2K_C L_C, \end{aligned} \tag{15}$$

$$\begin{aligned} m_S \frac{d^2(x_D + x_E)}{dt^2} &+ \gamma_S \frac{d(x_D + x_E)}{dt} + K_S(x_D + x_E) \\ &= f(x_D, x_E) + g(x_D, x_E) + K_S(x_A + x_B). \end{aligned} \tag{16}$$

Next we consider the force produced by the AAA+ ring and the force representing the binding affinities to the microtubule. From experimental measurements, we assume that a MTBD binds to binding sites that are 16 nm apart [36, 40]. We further assume that only one MTBD can bind to a binding site at any time and consider the microtubule as a one dimensional line with possible binding sites 8 nm apart. Let p_b, $b \in \mathbb{N}_0$, be the position of a binding site on a microtubule, where $p_{b+1} - p_b = 8$ (see Figure 5). Then we set p_{2b}, $b \in \mathbb{N}_0$ to be the binding sites for MTBD D and

p_{2b+1}, $b \in \mathbb{N}_0$ for MTBD E, respectively.

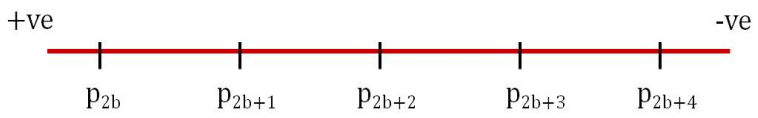

Figure 5: Diagram depicting the binding sites on the microtubule. Here the microtubule is modelled as a line. The +ve represents the cell membrane location and -ve the nucleus.

For simplicity, we model the force produced by the AAA+ ring using a heavy-side function. We use this function as the MTBD will alternate between having contact and no contact with the microtubule. Equally, we could use a periodic function. This forms part of our future studies. When the AAA+ ring B is in front we assume that the AAA+ ring A produce a constant force, $H > 0$, until it binds to the next binding site, p_{2b+2}. During this time we let AAA+ ring B produce no force. Equivalently, when the AAA+ ring A is in front we assume that the AAA+ ring B produce a constant force, H, until it binds to the next binding site, p_{2b+3}. During this time, we let AAA+ ring A produce no force (see Figure 6). Hence, for $b \in \mathbb{N}_0$ we write

$$F_A = \begin{cases} H, & p_{2b} \leq x_D < p_{2b+2},\ x_E = p_{2b+1}, \\ \\ 0, & p_{2b+1} \leq x_E < p_{2b+3},\ x_D = p_{2b+2}, \end{cases}$$

and

$$F_B = \begin{cases} 0, & p_{2b} \leq x_D < p_{2b+2},\ x_E = p_{2b+1}, \\ \\ H, & p_{2b+1} \leq x_E < p_{2b+3},\ x_D = p_{2b+2}, \end{cases}$$

respectively. It follows that

$$F_A + F_B \equiv H. \tag{17}$$

Now consider the binding force on the MTBD. We model this force again by a heavy-side function in the horizontal direction. Assume that there is only a single force when the MTBD is at the binding site and that this force acts in the horizontal direction, denoted here by G. Hence,

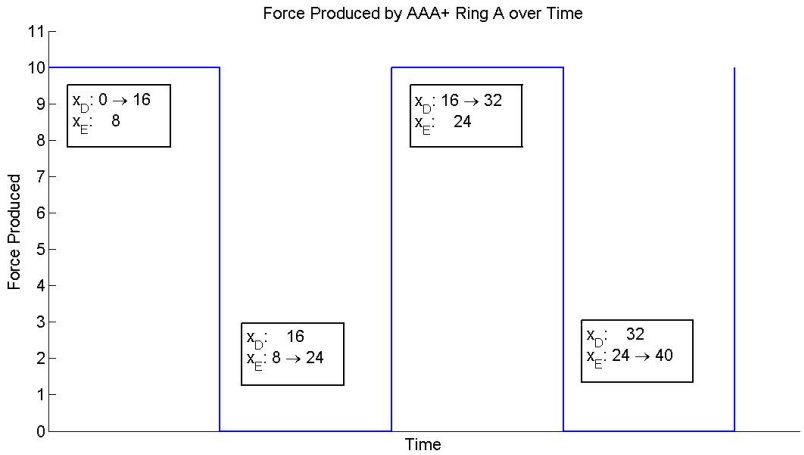

(a)

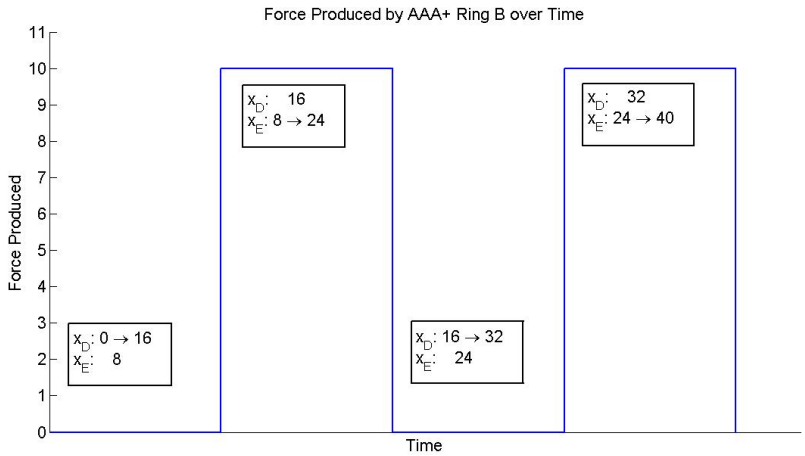

(b)

Figure 6: Graphs of the functions F_A and F_B representing the forces produced by AAA+ rings A and B respectively. Here we assume $x_D(0) = p_0 = 0$, $x_E(0) = p_1 = 8$ and $H = 10$ (see Table 1). (a) $F_A = 10$ when MTBD D moves from binding site $p_0 = 0$ to $p_2 = 16$, whilst MTBD E stays at binding site $p_1 = 8$. Then $F_A = 0$ when MTBD E moves from binding site $p_1 = 8$ to $p_3 = 24$, whilst MTBD E stays at binding site $p_2 = 16$. (b) $F_B = 0$ when MTBD D moves from binding site $p_0 = 0$ to $p_2 = 16$, whilst MTBD E stays at binding site $p_1 = 8$. Then $F_B = 10$ when MTBD E moves from binding site $p_1 = 8$ to $p_3 = 24$, whilst MTBD E stays at binding site $p_2 = 16$.

for $b \in \mathbb{N}_0$ we have

$$f(x_D, x_E) = \begin{cases} G & \text{if } x_D = p_{2b}, \\ 0 & \text{otherwise,} \end{cases}$$

and

$$g(x_D, x_E) = \begin{cases} G & \text{if } x_E = p_{2b+1}, \\ 0 & \text{otherwise,} \end{cases}$$

respectively. Furthermore, assume that when the MTBD in front binds to the microtubule, the other MTBD simultaneously unbinds, hence we will never have $x_D = p_{2b}$ and $x_E = p_{2b+1}$ simultaneously. In our model, if $x_E = p_{2b+1}$ then $x_D \neq p_{2b}$ and if $x_D = p_{2b}$ then $x_E \neq p_{2b+1}$. Hence,

$$f(x_D, x_E) + g(x_D, x_E) \equiv G. \tag{18}$$

Defining $x_M := x_A + x_B$ and $x_S := x_D + x_E$, and using (17) and (18) then equations (14) - (16) reduce to:

$$m_C \frac{d^2 x_C}{dt^2} + \gamma_C \frac{dx_C}{dt} + 2K_C x_C = K_C(x_M - 2L_C), \tag{19}$$

$$m_M \frac{d^2 x_M}{dt^2} + \gamma_M \frac{dx_M}{dt} + (K_C + K_S)x_M = 2K_C x_C + K_S x_S + 2K_C L_C + H, \tag{20}$$

$$m_S \frac{d^2 x_S}{dt^2} + \gamma_S \frac{dx_S}{dt} + K_S x_S = K_S x_M + G. \tag{21}$$

3.3 Non-dimensionalisation

We now proceed to non-dimensionalise the model system, given by equations (19) - (21). Let M, L and T denote mass, length and time respectively, with megadaltons, nanometers and seconds as the units of mass, length and time respectively. The dimensions of our parameters are:

$$[m_C] = [m_M] = [m_S] = M,$$

$$[\gamma_C] = [\gamma_M] = [\gamma_S] = MT^{-1},$$

$$[K_C] = [K_S] = MT^{-2},$$

$$[G] = [H] = MLT^{-2},$$

$$[L_C] = L.$$

The dimensions of our variables are:

$$[x_C] = [x_M] = [x_S] = L, \quad \text{and} \quad [t] = T.$$

Let us choose our characteristics as follows:

$$x_C = L_C \chi_C,\ x_M = \frac{H}{K_C + K_S}\chi_M,\ x_S = \frac{G}{K_S}\chi_S,\ \text{and} \quad t = \frac{\gamma_C}{K_C}\tau,$$

where χ_C, χ_M, χ_S and τ are dimensionless variables.

Substituting for these in equations (19) - (21) and simplifying gives:

$$\varepsilon_1 \frac{d^2\chi_C}{d\tau^2} + \frac{d\chi_C}{d\tau} + 2\chi_C = b_1\chi_M - 2, \tag{22}$$

$$\varepsilon_2 \frac{d^2\chi_M}{d\tau^2} + a_2\frac{d\chi_M}{d\tau} + \chi_M = b_2\chi_C + c_2\chi_S + d_2, \tag{23}$$

$$\varepsilon_3 \frac{d^2\chi_S}{d\tau^2} + a_3\frac{d\chi_S}{d\tau} + \chi_S = b_3\chi_M + 1, \tag{24}$$

where

$$\begin{aligned}
&\varepsilon_1 = \frac{m_C K_C}{{\gamma_C}^2}, \quad \varepsilon_2 = \frac{m_M {K_C}^2}{{\gamma_C}^2(K_C + K_S)}, \quad \varepsilon_3 = \frac{m_S {K_C}^2}{{\gamma_C}^2 K_S},\\
&a_2 = \frac{\gamma_M K_C}{\gamma_C(K_C + K_S)}, \quad a_3 = \frac{\gamma_S K_C}{\gamma_C K_S},\\
&b_1 = \frac{H}{L_C(K_C + K_S)}, \quad b_2 = \frac{2K_C L_C}{H}, \quad b_3 = \frac{K_S H}{G(K_C + K_S)},\\
&c_2 = \frac{G}{H} \qquad \text{and} \qquad d_2 = \frac{2K_C L_C}{H} + 1.
\end{aligned}$$

We note that, using the values of the parameters given in Table 1 we obtain:

$$\varepsilon_1 \le \frac{m_C}{144000\pi^2}, \quad \varepsilon_2 \le \frac{m_M}{14400\pi^2} \quad \text{and} \quad \varepsilon_3 \le \frac{m_S}{7200\pi^2}.$$

It is known that the mass of the dynein complex is 1.2 MDa [28] hence $m_S < 1.2$ and $m_M < 1.2$. To the authors' knowledge there are no experimental ranges for the mass of an endosome, hence a precise value for the model parameter m_C is unknown. However, for experimental purposes Qdots can be used for monitoring endocytosis in cells [27]. The largest Qdots, supplied by *Invitrogen - Life Technologies* [27], are 800 nm in size and have an estimated mass of 2 MDa. We assume that Qdots can approximate endosomes well in experiments and hence we take $m_C \le 2$. The above

upper bounds on the masses imply that $\varepsilon_1 \lll 1$, $\varepsilon_2 \lll 1$ and $\varepsilon_3 \lll 1$ and therefore from now on, we neglect the acceleration terms to obtain the following system of first order ordinary differential equations:

$$\frac{d\chi_C}{d\tau} + 2\chi_C = b_1\chi_M - 2, \tag{25}$$

$$\frac{d\chi_M}{d\tau} + a_4\chi_M = b_4\chi_C + c_4\chi_S + d_4, \tag{26}$$

$$\frac{d\chi_S}{d\tau} + a_5\chi_S = b_5\chi_M + a_5, \tag{27}$$

where

$$a_4 = \frac{\gamma_C(K_C + K_S)}{\gamma_M K_C}, \quad a_5 = \frac{\gamma_C K_S}{\gamma_S K_C},$$
$$b_1 = \frac{H}{L_C(K_C + K_S)}, \quad b_4 = \frac{2L_C\gamma_C(K_C + K_S)}{\gamma_M H}, \quad b_5 = \frac{\gamma_C {K_S}^2 H}{\gamma_S(K_C)G(K_C + K_S)},$$
$$c_4 = \frac{\gamma_C G(K_C + K_S)}{\gamma_M K_C H} \quad \text{and} \quad d_4 = \frac{\gamma_C(2K_C L_C + H)(K_C + K_S)}{\gamma_M K_C H}.$$

Remark 3.1 (Masses are dynamic quantities). We note that the endocytic pathway is very dynamic in nature. The masses of the dynein complex and the endosome are variable quantities due to the fact that their protein content is dynamic as a result of the recruitment and shedding of proteins at different stages of the pathway and each of the proteins involved will have different molecular weights. The endosomes will also contain variable numbers of receptor-ligand complexes. In future studies, we will consider dynamic masses, thereby giving rise to a system of second order ordinary differential equations. We leave this extension and others for future studies.

Remark 3.2 (Michaelis-Menten Constant). Note that we can identify an equivalent *Michaelis-Menten* constant defined by the spring constants. For example,

$$K_M = \frac{K_C + K_S}{K_C}.$$

3.4 Parameter values

Let us consider the damping coefficients. From Stokes' Law we have that

$$\gamma_C = 6\pi\mu R_C, \gamma_M = 6\pi\mu R_M \text{ and } \gamma_S = 6\pi\mu R_S$$

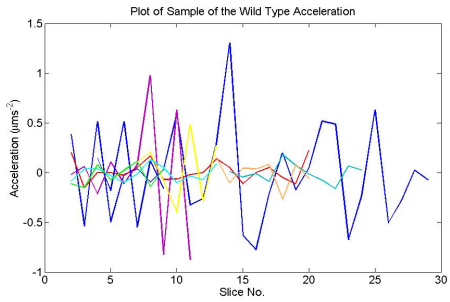

Figure 7: (Colour version online) Plot of a sample of accelerations from the individually tracked EGF movements in wild type cells, calculated using velocities obtained from ImageJ [9]; each tracked EGF movement is represented in a different colour. Live cell images were captured on a personal Delta Vision, at 2 sec intervals, 30 min post removal of EGF. A slice number of N represents the Nth image captured at a time of $2N$ sec. The plot shows that the accelerations have an oscillatory profile over time, with accelerations generally less than $1\mu ms^{-2}$.

where μ is the viscosity and R_C, R_M and R_S are the radii of the cargo, motor and microtubule-binding domain respectively. Hence, the coefficients in equations (25) - (27) can be simplified to:

$$a_4 = \frac{R_C(K_C + K_S)}{R_M K_C}, \quad a_5 = \frac{R_C K_S}{R_S K_C},$$
$$b_1 = \frac{H}{L_C(K_C + K_S)}, \quad b_4 = \frac{2L_C R_C(K_C + K_S)}{R_M H}, \quad b_5 = \frac{R_C {K_S}^2 H}{R_S(K_C)G(K_C + K_S)},$$
$$c_4 = \frac{R_C G(K_C + K_S)}{R_M K_C H} \quad \text{and} \quad d_4 = \frac{R_C(2K_C L_C + H)(K_C + K_S)}{R_M K_C H}.$$

Let us now consider the force G. In our model we want the AAA+ ring at the front to be stationary whilst the other AAA+ ring steps forward. During this time, the forces must balance. Given our previous assumptions we have:

$$G = \begin{cases} K_S(x_E - x_B) & \text{when AAA+ ring } B \text{ is in front,} \\ K_S(x_D - x_A) & \text{when AAA+ ring } A \text{ is in front,} \end{cases}$$

which holds at all time. Let us assume that initial conditions are given by $x_D(0) = p_0$ and $x_E(0) = p_1 = p_0 + 8$. Then we have for all time

$$G = K_S(p_0 + 8 - x_B(0)).$$

Note that we could equivalently assume that $x_D(0) = p_1 = p_0 + 8$ and $x_E(0) = p_0$ giving $G =$

$K_S(p_0 + 8 - x_A(0))$.

Our model parameters therefore consist of radii (R_C, R_M, R_S), spring constants (K_C, K_S), natural spring length (L_C) and force (H). The measured values of these parameters are given in Table 1.

Parameter	Meaning	Value	Ref.	Primary Value
R_C	Radius of the cargo	100-500 nm	[35]	100 nm
R_M	Radius of the AAA+ ring	6.5 nm	[6, 17]	6.5 nm
R_S	Radius of the MTBD	2-4 nm	[17]	3 nm
K_C	Spring constant between the cargo and the AAA+ ring	1-10 pN/nm	Estimated [22, 43]	1 pN/nm
K_S	Spring constant between the AAA+ ring and the MTBD	1-10 pN/nm	Estimated [22]	7 pN/nm
L_C	Unstressed length between the AAA+ ring and cargo	15-20 nm	Estimated [39]	20 nm
H	Force produced by the AAA+ ring	1-10 pN	[44]	10pN
μ	Viscosity of the cytoplasm	2-50 cP	[53]	2 cP

Table 1: Dimensional parameters, their given ranges and the primary values used in the mathematical model except where it is specified otherwise. Here we also include references for those parameter values we could find in the literature. The rest are estimated using plausible experimental ranges.

3.5 Initial Conditions

Turning to initial conditions, we take the initial position of the cargo to be zero for simplicity, that is $x_C = 0$. We have already assumed that $x_D(0) = p_0$ and $x_E(0) = p_0 + 8$; hence $x_S(0) = 2p_0 + 8$. We now take p_0 to be another parameter of our model. We assume that x_A and x_B must also start within the interval $[p_0, p_0 + 8]$. We choose to consider two possible situations. Either both

Coefficient	Value
a_4	123.0769
a_5	233.3333
b_1	0.0625
b_4	492.3077
b_5	72.9167
c_4	344.6154
d_4	615.3846

Table 2: Non-dimensional parameters and their values using the primary values of our dimensional parameters

AAA+ rings start symmetrically about $p_0 + 4$ nm or they start in exactly the same point, i.e. one is directly behind the other as we face the motor. We assume that AAA+ ring A is the backward AAA+ ring in the first scenario and take its initial position to be the unstressed length of the spring between the AAA+ ring and the cargo. In the second scenario we take the initial position of both motors to be the unstressed length of the spring between the AAA+ ring and the cargo. Let A be a parameter representing our assumption on the respective initial positions of the AAA+ rings. If $A = 0$ then we are assuming that the AAA+ rings are symmetric about $p_0 + 4$ nm and if $A = 1$ we assume that they start in exactly the same position. The initial condition for x_M is then given by

$$x_M(0) = \begin{cases} 2p_0 + 8, & A = 0, \\ 2L_C, & A = 1. \end{cases}$$

Note that our standard initial condition will be $p_0 = L_C - 4$, giving $x_M(0) = 2L_C$ independently of A.

Since we are solving the non-dimensional model, we must also non-dimensionalise these conditions. Using the characteristics given in section 3.3 we set our initial conditions to be $\chi_C(0) = 0$

$$\chi_M(0) = \begin{cases} \frac{(2p_0+8)(K_C+K_S)}{H}, & A = 0, \\ \frac{2L_C(K_C+K_S)}{H}, & A = 1, \end{cases}$$

and $\chi_S(0) = \frac{(2p_0+8)K_S}{G}$. Using our definition of G this simplifies to

$$\chi_S(0) = \begin{cases} \frac{2p_0+8}{L_C-p_0}, & A = 0, \\ \frac{2p_0+8}{p_0+8-L_C}, & A = 1. \end{cases}$$

4 Analysis of the model equations

In this section we will analyse the system of equations:

$$\begin{cases} \frac{d\chi_C}{d\tau} + 2\chi_C = b_1\chi_M - 2, \\ \frac{d\chi_M}{d\tau} + a_4\chi_M = b_4\chi_C + c_4\chi_S + d_4, \\ \frac{d\chi_S}{d\tau} + a_5\chi_S = b_5\chi_M + a_5, \\ \text{given initial conditions:} \\ \chi_C(0) = 0, \\ \chi_M(0) = \begin{cases} \frac{(2p_0+8)(K_C+K_S)}{H} & A = 0 \\ \frac{2L_C(K_C+K_S)}{H} & A = 1, \end{cases} \\ \chi_S(0) = \begin{cases} \frac{2p_0+8}{L_C-p_0} & A = 0 \\ \frac{2p_0+8}{p_0+8-L_C} & A = 1, \end{cases} \end{cases} \tag{28}$$

with coefficients as given in section 3.3 with parameter values given in Table 1 and as described in Section 3.4.

4.1 Steady States

We consider the steady states of the model system (28). Steady states will satisfy

$$\frac{d\chi_C}{d\tau} = \frac{d\chi_M}{d\tau} = \frac{d\chi_S}{d\tau} = 0.$$

Substituting for these in the system (28) we obtain:

$$2\chi_C = b_1\chi_M - 2, \tag{29}$$

$$a_4\chi_M = b_4\chi_C + c_4\chi_S + d_4, \tag{30}$$

$$a_5\chi_S = b_5\chi_M + a_5. \tag{31}$$

From equations (29) and (31) we have:

$$\chi_C = \frac{b_1}{2}\chi_M - 1 \quad \text{and} \quad \chi_S = \frac{b_5}{a_5}\chi_M + 1.$$

Substituting for χ_C and χ_S in equation (30) gives:

$$\begin{aligned} a_4\chi_M &= b_4\Big(\frac{b_1}{2}\chi_M - 1\Big) + c_4\Big(\frac{b_5}{a_5}\chi_M + 1\Big) + d_4 \\ &\Rightarrow \chi_M\Big[a_4 - \frac{b_1 b_4}{2} - \frac{c_4 b_5}{a_5}\Big] = c_4 + d_4 - b_4. \end{aligned} \tag{32}$$

Using the definitions of the coefficients (see section 3.3) we obtain:

$$\begin{aligned} a_4 - \frac{b_1 b_4}{2} - \frac{c_4 b_5}{a_5} &= \frac{\gamma_C(K_C+K_S)}{\gamma_M K_C} - \Big(\frac{H}{2L_C(K_C+K_S)}\Big)\Big(\frac{2L_C\gamma_C(K_C+K_S)}{\gamma_M H}\Big) \\ &\quad -\Big(\frac{\gamma_C G(K_C+K_S)}{\gamma_M H K_C}\Big)\Big(\frac{\gamma_C H {K_S}^2}{\gamma_M G K_C(K_C+K_S)}\Big)\Big(\frac{\gamma_S K_C}{\gamma_C K_S}\Big), \\ &= \frac{\gamma_C}{\gamma_M}\Big[\frac{K_C+K_S}{K_C} - 1 - \frac{K_S}{K_C}\Big], \\ &= 0. \end{aligned}$$

Now consider the right hand side of equation (32). Again from the definitions of the coefficients we have:

$$\begin{aligned} c_4 + d_4 - b_4 &= \frac{\gamma_C G(K_C+K_S)}{\gamma_M H K_C} + \frac{\gamma_C(2K_C L_C + H)(K_C+K_S)}{\gamma_M H K_C} - \frac{2L_C\gamma_C(K_C+K_S)}{\gamma_M H}, \\ &= \frac{\gamma_C}{\gamma_M H}\Big[\frac{G(K_C+K_S)}{K_C} + \frac{(2K_C L_C + H)(K_C+K_S)}{K_C} - 2L_C(K_C+K_S)\Big], \\ &= \frac{\gamma_C(K_C+K_S)}{\gamma_M H K_C}\Big[G+H\Big]. \end{aligned}$$

Hence, if $G = -H$ then we will have infinite solutions to equations (29) to (31) otherwise we will have no solutions. Due to our previous assumptions (see section 3) we have $G \geq 0$ and $H > 0$, hence $G \neq -H$ and we therefore have no steady states. This is to be expected; we have derived a model in which dynein is expected to continually move along the microtubule.

5 Numerical Simulations

5.1 Numerical Approximate Solutions of the Model Equations

We proceeded to solve the system of equations (28) using MATLAB solver *ode45*. The solver *ode45* is a MATLAB function which solves initial value problems for ordinary differential equations [34]. We initially chose to solve over an interval of 0 to 1860 seconds, based on the available experimental

data. By using the characteristic for the time scale, given in Section 3.3, we solved the system over the interval [0,T] such that $T = \frac{1860K_C}{6\pi\mu R_C}$. We set the parameters to have their primary values as given in Table 1 and $p_0 = L_C - 4$ where we can take $A = 0$ or $A = 1$.

We also considered the velocity of the cargo, which is our main focus due to the experimental data available. Our results for the trajectory of the variable relating to the cargo were discrete and hence we approximated the velocity by the following:

$$\frac{dx}{dt} = v_{n+1} \approx \frac{x_{n+1} - x_n}{t_{n+1} - t_n},$$

where $X = \{x_n\}$ is the matrix for the trajectory and $T = \{t_n\}$ is the dimensionless time matrix.

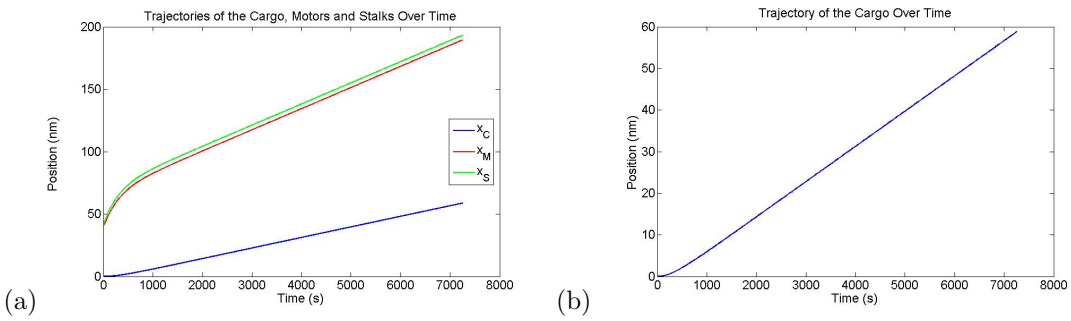

Figure 8: (Colour version online) Graphs of the dimensional trajectories over time; given by solving the model equations (28) and dimensionalising the solutions, with all parameters equal to the primary values. (a) Plot of the trajectories of the AAA+ rings, MTBDs and the cargo over time. (b) Plot of the trajectory of the cargo over time.

We proceeded to dimensionalise our solution, obtained using the primary values of our parameters, in order to make comparisons with the experimental data (see Figure 8). We plot the results using MATLAB, first with all three trajectories on one graph and then with just the trajectory of the variable relating to the cargo. As expected, the AAA+ rings and MTBDs follow similar trajectories, with the trajectory for the MTBDs slightly above that for the AAA+ rings with the same gradient. The trajectory of the cargo follows a path with a lower gradient than that of the AAA+ rings and the MTBDs, indicating a lower velocity. Here we must note that the trajectory of the MTBDs is the sum of the trajectories for both MTBDs, and similarly the trajectory of the AAA+ rings is the sum of the trajectories for both AAA+ rings. The profile of the velocity of the cargo, after the initial high acceleration, resembles qualitatively the oscillations seen in the results obtained by experimental assays (see Figure 9). We also extended the time interval for which the solution was obtained up to 7260 seconds to analyse the solution over a longer period.

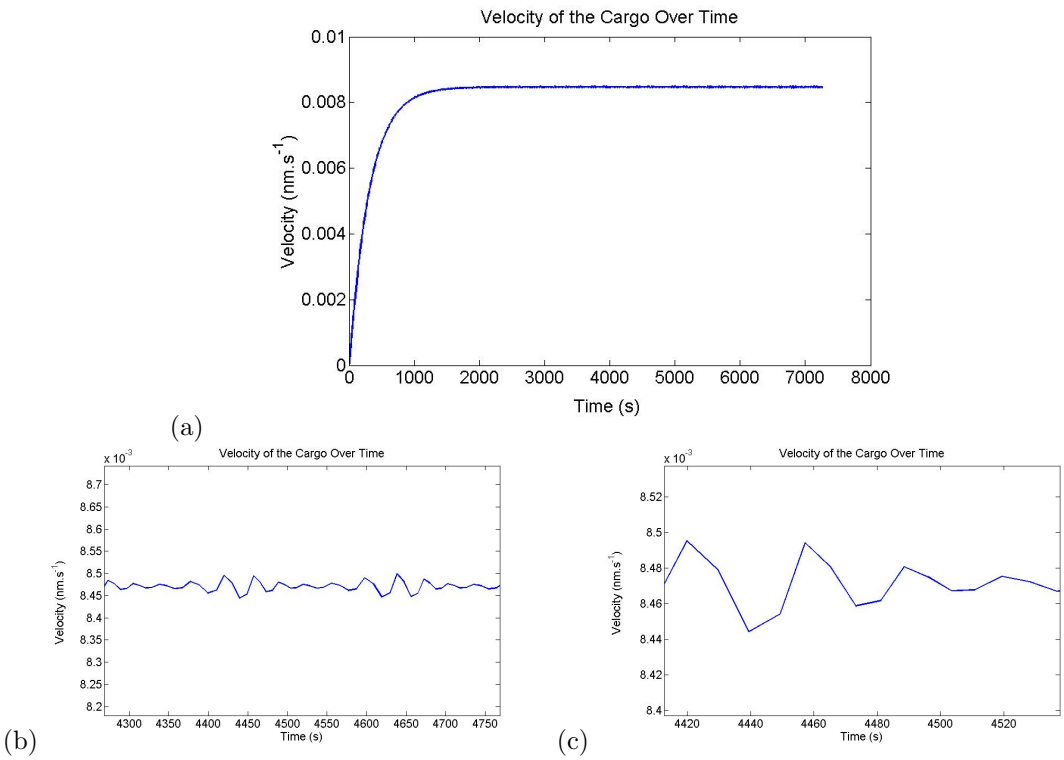

Figure 9: (Colour version online) Graphs of the dimensional velocities of the cargo over time; given by solving the model equations (28) and dimensionalising the solutions, with all parameters equal to the primary values. (a) Plot of the velocity of the cargo over time. (b) Section of the velocity profile of the cargo over time. (c) Sub-section of the velocity profile of the cargo over time.

The trajectories continue in the same manner and the velocity remains in a band with a similar oscillatory pattern. We note that time-stepping refinement does not alter the quantitative nature of the solutions. Hence, the numerical method is robust and accurate.

5.2 Variation of Parameters

We studied the model equations by investigating the impact changes in parameter values on the trajectories and velocity. We considered variations in all the parameters except the radius of the AAA+ ring, which had a specific measured value rather than a measured range, and the viscosity of the cytoplasm, which only impacted on the dimensionalisation of our model. In each case we kept all other parameters constant at their primary value and varied one parameter within the range given (see Table 1). For p_0 we take $p_0 = L_C - 4$, which holds when $A = 0$ and $A = 1$, and then we vary p_0 with $L_C - 4 \leq p_0 < L_C$ for $A = 0$ and $L_C - 8 < p_0 \leq L_C$ for $A = 1$. Note that we use the strict inequalities in order to prevent the force from the binding affinity being equal to

zero. We computed solutions for several values within these ranges, however for clarity, the results presented here use the lowest, highest and primary values, extending up to a maximum of five values when considered necessary.

- **Vary R_C:** The radius of the cargo was found to be in a range of 100 to 500 nm (see Table 1). We found that an increase of the radius of the cargo led to an increase in the velocity and lower distance travelled for the non-dimensional variable representing the cargo (see Figure 10(a)) and a decreased distance travelled for the MTBDs and AAA+ rings. This is what we would intuitively expect as this means that the motor protein is transporting a smaller object which we would expect to have less resistance in a viscous medium.

- **Vary R_S:** The radius of the MTBD was found to range between 2 to 4 nm (see Table 1). We found that a higher radius would lead to a lower velocity and shorter distance travelled for the non-dimensional cargo variable, but this change was very small (see Figure 10(b)). It also had a very small impact on the trajectories for the MTBDs and AAA+ rings with a higher radius leading to a slightly lower distance travelled. This is intuitively what we would expect due to a smaller object experiencing less resistance.

- **Vary L_C:** The unstressed spring length connecting the cargo and AAA+ ring was found to be between 15 to 20 nm (see Table 1). We found that the longer the unstressed spring length the lower the velocity and distance travelled for the non-dimensional cargo variable, having a sizeable impact (see Figure 10(c)). An increased unstressed spring length also caused the trajectories for the variables representing the AAA+ rings and MTBDs to shift upwards, leading to an increased distance travelled and hence it is an important parameter.

- **Vary H:** The force produced by the AAA+ ring can range between 1 and 10 pN (see Table 1). As expected, the trajectories and velocity are significantly affected by variation in this parameter. The higher the force produced the higher the velocity of the non-dimensional cargo variable and the further distance travelled (see Figure 11(a)). A higher force produced also led to a higher distance travelled for the MTBDs but a lower distance for the AAA+ rings. The effect of a change in the force produced on the velocity and trajectories means that this force is a significant parameter in the model.

- **Vary K_C:** The spring constant connecting the cargo to the AAA+ ring was estimated to be between 1 and 10 pN/nm (see Table 1). Variation in the spring constant has a significant

impact on the velocities and distances travelled. The lower the spring constant, the higher the velocity and shorter distance travelled of the non-dimensional variable representing cargo (see Figure 11(b)). However, translating this to its effect on the velocity of the cargo would need further consideration since we use this parameter to non-dimensionalise time. A lower spring constant also gives a larger distance travelled for the MTBDs, but a shorter distance travelled for the AAA+ rings. This parameter is certainly significant for the non-dimensional model and is likely to be significant for the dimensional model.

- **Vary K_S:** The spring constant of the spring connecting the AAA+ ring to the MTBD was estimated to be between 1 and 10 pN/nm (see Table 1). Variation in this spring constant had a significant impact on the solutions, with a lower spring constant giving a lower velocity and a shorter distance travelled (see Figure 11(c)). This shows that further investigation into the true measurement of this spring constant would benefit the model.

- **Vary A and p_0:**

  (i) We assume that the AAA+ rings are initially symmetric about $p_0 + 4$ nm. We then vary p_0 such that $L_C - 4 \leq p_0 < L_C$. Variations in these initial conditions impacted on the solutions as we would expect. A lower initial condition for the AAA+ rings leads to a higher trajectory for the non-dimensional cargo and an increased velocity (see Figure 12(a)). As the initial condition got closer to L_C the trajectory converged to a straight line and the velocity curve flattened. A lower initial condition also gives a higher trajectory for the AAA+ rings, with an increased distance travelled, but lower trajectories for the non-dimensional MTBDs.

  (ii) We assume that the AAA+ rings are initially at the same point. We can then vary p_0 such that $L_C - 8 < p_0 \leq L_C$. Varying p_0 shows that a fall in the initial condition for the AAA+ rings gives a lower trajectory for the non-dimensional cargo, with a shorter distance travelled and a decrease in velocity (see Figure 12(b)). A lower initial condition also leads to a lower trajectory for the AAA+ rings, but a higher trajectory for the MTBDs, with a further distance travelled.

In summary, we have found that the parameters most significant for the model are the unstressed spring length connecting the cargo to the AAA+ ring, the force produced by the AAA+ ring and the spring constant connecting the AAA+ ring and the MTBD.

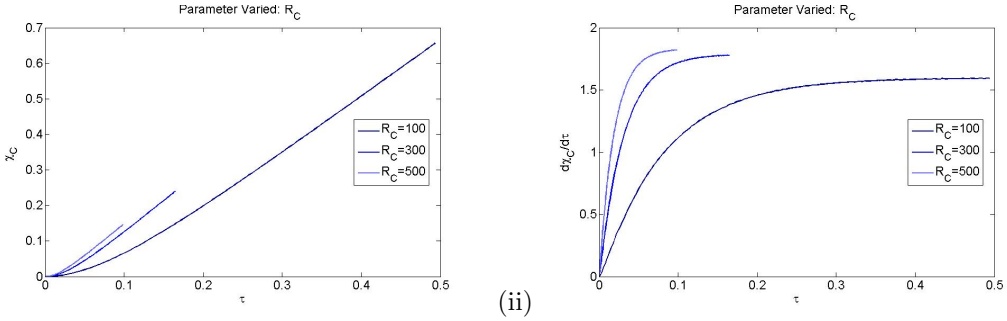

(i) (ii)

(a) Varying the radius of the cargo, setting it equal to 100nm, 300nm and 500nm. An increase of the radius of the cargo led to an increase in the velocity for the non-dimensional cargo variable and a shorter distance travelled for all variables. Note that the curves end at different points as we use the radius of the cargo to non-dimensionalise time.

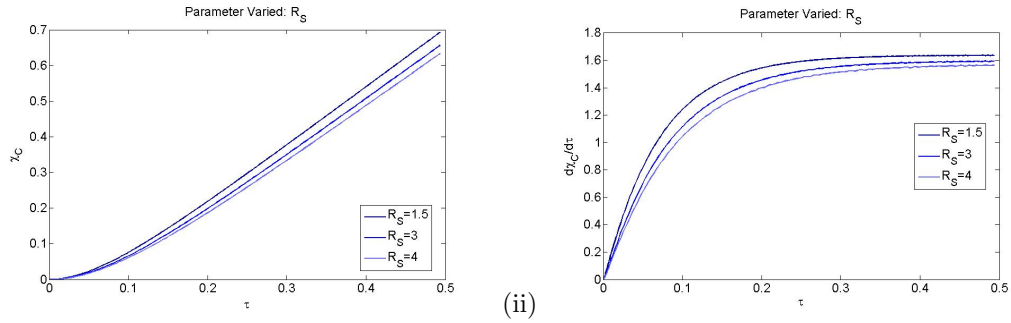

(i) (ii)

(b) Varying the radius of the MTBD, setting it equal to 1.5nm, 3nm and 4nm. An increase of the radius of the MTBD led to an decrease in the velocity for the non-dimensional cargo variable and a shorter distance travelled for all variables.

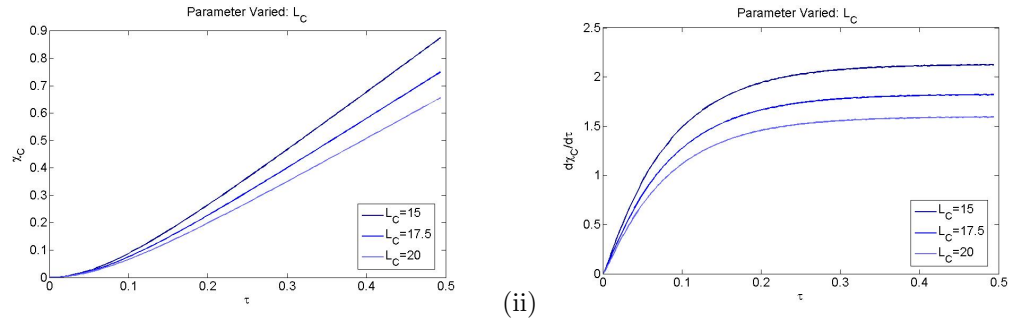

(i) (ii)

(c) Varying the unstressed spring length connecting the cargo to the AAA+ ring, setting it equal to 15nm, 17.5nm and 20nm. An increase in the unstressed spring length led to an decrease in the velocity for the non-dimensional cargo variable and a shorter distance travelled.

Figure 10: Graphs of the solutions to the model equations (28) in which we vary one identified parameter, R_C, R_S and L_C respectively, whilst all other parameters remain fixed at their primary values. (a)-(c): (i) Trajectory of the non-dimensional cargo variable over the non-dimensional time variable. (ii) Velocity of the non-dimensional cargo variable over the non-dimensional time variable.

6 Discussion: Biological justification of the model outcomes

The model accurately describes the processivity of cytoplasmic dynein and we have shown that the velocity profile of the solution to the model qualitatively matches experimental observations, hence our model is consistent with experiments. It must be noted that the magnitudes seen in our

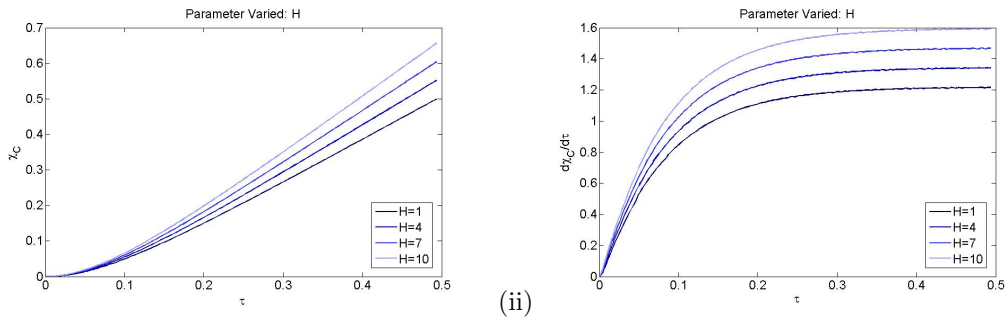

(i) (ii)

(a) Varying the force produced by the AAA+ ring, setting it equal to 1pN, 4pN, 7pN and 10pN. An increase in the force led to an increase in the velocity for the non-dimensional cargo variable and a further distance travelled.

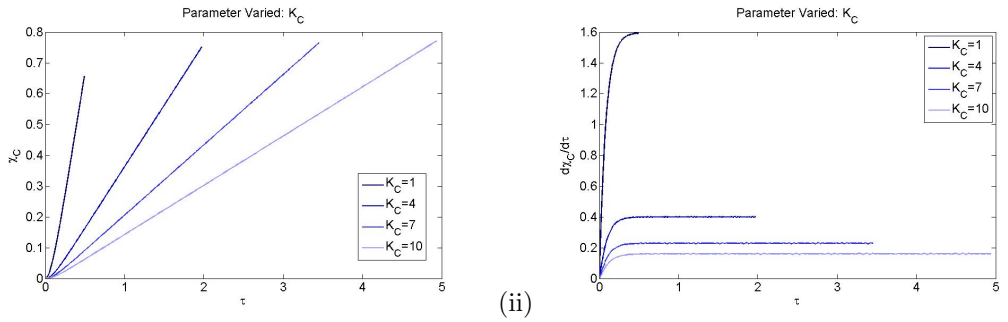

(i) (ii)

(b) Varying the spring constant of the spring connecting the cargo to the AAA+ ring, setting it equal to 1pN/nm, 4pN/nm, 7pN/nm and 10pN/nm. An increase in the spring constant led to a decrease in the velocity but a further distance travelled for the non-dimensional cargo variable.

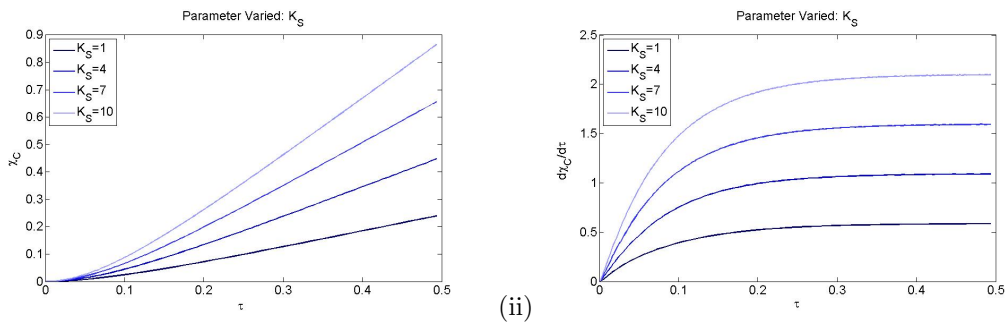

(i) (ii)

(c) Varying the spring constant connecting the AAA+ ring to the MTBD, setting it equal to 1pN/nm, 4pN/nm, 7pN/nm and 10pN/nm. An increase in the spring constant led to an increase in the velocity for the non-dimensional cargo variable and a further distance travelled.

Figure 11: Graphs of the solutions to the model equations (28) in which we vary one identified parameter, H, K_C and K_S respectively, whilst all other parameters remain fixed at their primary values. (a)-(c): (i) Trajectory of the non-dimensional cargo variable over the non-dimensional time variable. (ii) Velocity of the non-dimensional cargo variable over the non-dimensional time variable.

results do not match qualitatively those seen in the experiments. This could be due to the lack of experimental data on some of the parameters, such as the spring constants, or due to the presence of multiple dyneins in action on the cargo. The variables representing the cargo, AAA+ rings and MTBDs all progressively move along the microtuble. This is important as dynein will stay as one entity and should not have parts located at large distances away from each other. The variables

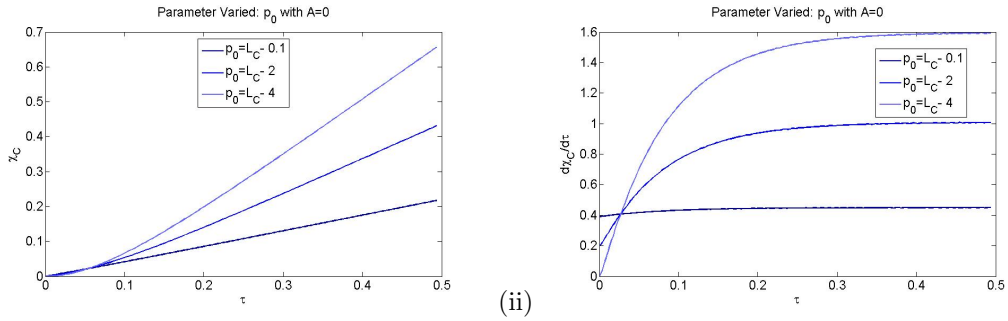

(i) (ii)

(a) Varying the parameter representing the binding site at which MTBD D is initially located, whilst we assume that the motors are initially positioned symmetrically about $p_0 + 4$ nm, setting p_0 equal to $L_C - 0.1$ nm , $L_C - 2$ nm and $L_C - 4$ nm. A lower initial condition for the AAA+ rings leads to a higher trajectory for the non-dimensional cargo and an increased velocity.

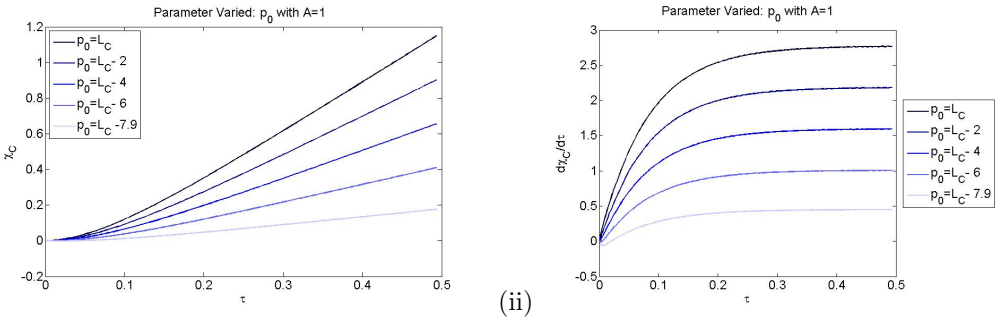

(i) (ii)

(b) Vary the parameter representing the binding site at which MTBD D is initially located, whilst we assume that the motors are initially positioned at the same point, p_0, setting p_0 equal to L_C nm, $L_C - 2$ nm, $L_C - 4$ nm, $L_C - 6$ nm and $L_C - 7.9$ nm. Varying p_0 shows that a fall in the initial condition for the AAA+ rings gives a lower trajectory and a decrease in the velocity for the non-dimensional cargo variable.

Figure 12: Graphs of the solutions to the model equations (28) in which we vary p_0 and A whilst all other parameters remain fixed at their primary values. (a)-(c): (i) Trajectory of the non-dimensional cargo variable over the non-dimensional time variable. (ii) Velocity of the non-dimensional cargo variable over the non-dimensional time variable.

that represent the MTBDs and AAA+ rings follow trajectories that are steeper and higher than those of the cargo variable. However, this is to be expected as the trajectories for the AAA+ rings and MTBDs are summations of the two components, hence we would expect the velocity and distance travelled to be twice that of the cargo. This is what we observe in the results. We also observe that the trajectories for the MTBDs and that for the AAA+ rings, after an initial increase, move with the same gradient; with the MTBDs slightly ahead of the AAA+ rings at any point in time. This holds even when we vary the initial conditions to account for different starting points of the AAA+ rings and in different positions, i.e. symmetric or together.

The results show that dynein moves the cargo progressively. In experiments on dynein alone, is seen to move progressively, however it is a simplification of what is seen in experiments on the dynein moving cargo. Experiments do show cargos within a cell being moved in the direction of the nucleus over time, however there are also pauses in movement and the cargo can travel backwards or

move in a direction which is not solely radial [21, 12, 42, 46]. Currently, the available experimental data does not show how the dynein itself is behaving at these times, as we only see the position of the endosome. The pauses and retrograde transport may be a result of the action of kinesins on the cargo, either in a tug-of-war scenario, dynein may occasionally fall off a microtubule, or simply become inhibited by a crowded cytoplasm [1, 21, 38, 42, 48]. In addition, non-radial movement, could also be a result of dynein being detached from the cargo or the microtubule. However, our model is aimed to capture only the movement of dynein when it is attached to the cargo and the microtubule, hence we would not expect it to capture these features.

One important assumption that we have made is that the mass of the cargo remains constant. This can only be applied to sections of the process of endocytosis. It is known that during the transport process from the cell membrane to the nucleus, the endosome will experience drastic changes to it mass from fusion and fission along the pathway. Here we have proposed the simplest model sufficient to capture the main features of dynein related transport which can be later adapted to incorporate the more complex features. As a model of dynein moving cargo for a short distance it is an effective model which accurately describes the transport process and is in agreement with experimental observations on these scales. The quantitative accuracy of the model could be improved through further research into the true values of the parameters as well as by incorporating more realistic features of the transport process.

The main biological implications of our model would be to use it to predict the effects of different mutations of dynein on distance travelled and velocity. Mutation could be effectively modelled through a change in one or more of the parameters, depending on how the mutation affected the dynein structure and its movement. For example, a mutation which reduced the force produced by the AAA+ ring would be represented by a decrease in the parameter H. In our model this would lead to a shorter distance travelled and lower velocity of the cargo. Studies on cells isolated from patients and the Loa mouse model suggest impaired affinity between cytoplasmic dynein and its cargo and microtubules [10, 20, 39]. These could be represented in our model as a fall in the parameters K_C and K_S respectively, which would consequently reduce the force associated with the binding affinity, thus leading to a shorter distance travelled and lower velocity of the cargo.

7 Conclusion and Future Research

In conclusion, we have derived from first principles a new mechanical model for the dynein mediated transport of endosomes. The model accurately describes the processivity of cytoplasmic dynein and we have shown that the velocity profile of the solution to the model qualitatively matches the experimental observations. We have also found parameters that could potentially be altered to affect the velocity and distance travelled of the endosome; and these are primarily the force produced by the AAA+ ring, the unstressed spring length, and the spring constant which represents the stalk. Our model would also benefit from further research into these parameters.

The potential for future research is great, with a vast number of possible extensions to the model. We made various simplifying assumptions in our model which could be relaxed. For example, the model could be developed to incorporate a lever motion of the stalk or ATP hydrolysis. We could also allow changes in the size of the cargo in order to account for the fission and fusion process of the endosome. The scope of the model could be widened by including the possibility that dynein detaches from the cargo or microtubule, or switches to another microtubule. We could also account for the effects of multiple motors attaching to the cargo. However, the main goal of future research would be to adapt our model to take into account mutations in cytoplasmic dynein such as those found to cause Charcot-Marie-Tooth disease and spinal muscular atrophy in humans and neurodegeneration in mouse models [8, 14, 19, 51].

Acknowledgements: LC was supported by a University of Sussex Junior Research Fellowship 2011. AM would like to acknowledge grant financial support from the LMS (*R4P2*), EPSRC (*EP/H020349/1*), the Royal Society Travel grant (*R4K1*), the Royal Society Research Grant (*R4N9*) and the British Council through its *UK-US New Partnership Fund as part of the Strategic Alliances and Partnerships strand of the Prime Ministers Initiative for International Education 2 (PMI2).* MH and CG would like to acknowledge financial support from the BBSRC (*BB/D526861/1*).

References

[1] S. Ally, A.G. Larson, K. Barlan, S.E. Rice and V.I. Gelfand, (2009). Opposite-polarity motors activate one another to trigger cargo transport in live cells. J Cell Biol 187, 1071-1082.

[2] P. Ashwin, C. Lin, and G. Steinberg, (2010), Queuing Induced by Bidirectional Motor Motion Near the End of a Microtubule, Physical Review E 82, 051907.

[3] E. Bananis, S. Nath, K. Gordon, P. Satir, R.J. Stockert, J.W. Murray, and A.W. Wolkoff, (2004), Microtubule-Dependent Movement of Late Endocytic Vesicles In Vitro: Requirements for Dynein and Kinesin, Molecular Biology of the Cell 15, 3688-3697.

[4] M. Bier, and F.J. Cao, (2011), How Occasional Backstepping Can Speed up a Processive Motor Protein, BioSystems 103, 355-359.

[5] C.L. Brown, K.C. Maier, T. Stauber, L.M. Ginkel, L. Wordeman, I. Vernos, and T. A. Schroer, (2005), Kinesin-2 is a Motor for Late Endosomes and Lysosomes, Traffic 6, 1114-1124.

[6] S.A. Burgess, M.L. Walker, H. Sakakibara, P.J. Knight, and K. Oiwa, (2003), Dynein Structure and Power Stroke, Nature 421, 715-718.

[7] A.P. Carter, C. Cho, L. Jin, and R.D. Vale, (2011), Crystal Structure of the Dynein Motor Domain, Science 331, 1159-1165.

[8] X.J. Chen, E.N. Levedakou, K.J. Millen, R.L. Wollmann, B. Soliven, and B. Popko, (2007) Proprioceptive Sensory Neuropathy in Mice with a Mutation in the Cytoplasmic Dynein Heavy Chain 1 Gene, Journal of Neuroscience 27(52), 14515-24.

[9] F. Cordelierés (2005) Manual Tracking, [accessed online], http://rsbweb.nih.gov/ij/plugins/track/track.html

[10] W. Deng, C. Garrett, B. Dombert, V. Soura, G. Banks, E.M.C. Fisher, M.P. van der Brug, (2010), Neurodegenerative Mutation in Cytoplasmic Dynein Alters Its Organization and Dynein-Dynactin and Dynein-Kinesin Interactions. Journal of Biological Chemistry, 285(51), 3992239934. doi:10.1074/jbc.M110.178087.

[11] A. Dinh, C. Pangarkar, T. Theofanous, and S. Mitragotri, (2006), Theory of Spatial Patterns of Intracellular Organelles, Biophysical Journal: Biophysical Letters, L67-L69.

[12] O.J. Driskell, A. Mironov, V.J. Allan, and P.G. Woodman, (2007), Dynein is Required for Receptor Sorting and the Morphogenesis of Early Endosomes, Nature Cell Biology 9(1), 113-120.

[13] J.W. Driver, A.R. Rogers, D.K. Jamison, R.K. Das, A.B. Kolomeisky, and M.R. Diehl, (2010), Coupling Between Motor Proteins Determines Dynamic Behaviours of Motor Protein Assemblies, Physical Chemistry Chemical Physics 12, 10398-10405.

[14] L.W. Duchen, (1974), A Dominant Hereditary Sensory Disorder in the Mouse with Deficiency of Muscle Spindles: The Mutant Sprawling, Journal of Physiology 237(2), 10P-11P.

[15] A. Friedman, and G. Cracium, (2005), A Model of Intracellular Transport of Particles in an Axon, Journal of Mathematical Biology 80, 217-246.

[16] Y. Gao, C.C. Hubbert, and T. Yao, (2010), The Microtubule-Associated Histone Deacetylase 6 (HDAC6) Regulates Epidermal Growth Factor Receptor (EGFR) Endocytic Trafficking and Degradation, The Journal of Biological Chemistry 285(15), 11219-11226.

[17] M.A. Gee, J.E. Heuser, and R.B. Vallee, (1997), An Extended Microtubule-Binding Structure within the Dynein Motor Domain, Nature 390, 636-639.

[18] J. Gruenberg, (2001), The Endocytic Pathway: A Mosaic of Domains, Nature Reviews: Molecular Cell Biology 2, 721-730.

[19] M. Hafezparast, R. Klocke, C. Ruhrberg, A. Marquardt, A. Ahmad-Annuar, S Bowen, G. Lalli, A.S. Witherden, H. Hummerich, S. Nicholson, P.J. Morgan, R. Oozageer, J.V. Priestley, S. Averill, V.R. King, S. Ball, J. Peters, T. Toda, A. Yamamoto, Y. Hiraoka, M. Augustin, D. Korthaus, S. Wattler, M. Wabnitz, P. Dickneite, C. Lampe, S. Boehme, F. Peraus, G. Popp, A. Rudelius, M. Schlegel, J. Fuchs, H. Hrabe de Angelis, G. Schiavo, D.T. Shima, A.P. Russ, G. Stumm, J.E. Martin, and E.M.C. Fisher, (2003), Mutations in Dynein Link Motor Neuron Degeneration to Defects in Retrograde Transport, Science 300(5620), 808-812.

[20] Harms, M. B., Ori-McKenney, K. M., Scoto, M., Tuck, E. P., Bell, S., Ma, D., Masi, S., (2012), Mutations in the tail domain of DYNC1H1 cause dominant spinal muscular atrophy. Neurology. doi:10.1212/WNL.0b013e3182556c05.

[21] A.G. Hendricks, J.E. Lazarus and E.L. Holzbaur, (2010), Dynein at odd angles? Nat Cell Biol 12, 1126-1128.

[22] A.G. Hendricks, B.I. Epureanu, and E. Meyhöfer, (2008), Mechanistic Mathematical Model of Kinesin Under Time and Space Fluctuating Loads, Nonlinear Dynamics 53, 303-320.

[23] S. Hoepfner, F. Severin, A. Cabezas, B. Habermann, A. Runge, D. Gilooly, H. Stenmark, and M. Zerial, (2005), Modulation of Receptor Recycling and Degradation by the Endosomal Kinesin K1F16B, Cell 121, 437-450.

[24] J. Howard, (2001), Mechanics of Motor Proteins and the Cytoskeleton, Sinauer Associates Inc, Sunderland, USA.

[25] Y. Imafuku, N. Thomas and K. Tawada, (2009), Hopping and Stalling of Processive Molecular Motors, Journal of Theoretical Biology 261, 43-49.

[26] K. Imamula, T. Kon, R. Ohkura and K. Sutoh, (2009), The coordination of cyclic microtubule association/dissociation and tail swing of cytoplasmic dynein. Proc Natl Acad Sci U S A 104, 16134-16139.

[27] Invitrogen - Life Technologies, (2012), Life Technologies Corporation [accessed online] http://www.lifetechnologies.com/global/en/home.html

[28] T. Kon, K. Sutoh, and G. Kurisu, (2011), X-ray Structure of a Functional Full-length Dynein Motor Domain, Nature Structural and Molecular Biology 18(6), 638-643.

[29] C. Korn, S. Klumpp, R. Lipowsky, and U. S. Schwarz, (2009), Stochastic Simulations of Cargo Transport by Processive Molecular Motors, The Journal of Chemical Physics 131, 245107.

[30] A. Kunwar, M. Vershinin, J. Xu, and S.P. Gross, (2008), Stepping, Strain Gating, and an Unexpected Force-Velocity Curve for Multiple-Motor-Based Transport, Current Biology 18, 1173-1183.

[31] A.V. Kuznetsov, and K. Hooman, (2008), Modelling Traffic Jams in Intracellular Transport in Axons, International Journal of Heat and Mass Transfer 51, 5695-5699.

[32] A.V. Kuznetsov, (2011), Coupling a Dynein Transport Model with a Model of Anterograde and Retrograde Transport of Intracellular Organelles, International Communications in Heat and Mass Transfer 38, 833-837.

[33] S. Lubery, C. Wilhelm, I. Hurbain, S. Neveu, D. Louvard, and E. Coudrier, (2008), Different Microtubule Motors Move Early and Late Endocytic Compartments, Traffic 9, 492-509.

[34] MathWorks, (2011), MATLAB Product Documentation, [accessed online], http://www.mathworks.co.uk/help/techdoc/ref/ode45.html

[35] S. Mitragotri, and J. Lahann, (2009), Physical Approaches to Biomaterial Design, Nature Materials 8, 15-23.

[36] S. Mukherji, (2008), Model for Unidirectional Motion of a Dynein Molecule, Physical Review E 77, 051916.

[37] J. Munárriz, J.J. Mazo, and F. Falo, (2008), Model for Hand-Over-Hand Motion of Molecular Motors, Physical Review E 77, 031915.

[38] J.W. Murray, and A.W. Wolkoff, (2003), Roles of the Cytoskeleton and Motor Proteins in Endocytic Sorting, Advanced Drug Delivery Reviews 55, 1385-1403.

[39] K.M. Ori-McKenney, J. Xu, S.P. Gross, R.B. Vallee, (2010), A Cytoplasmic Dynein Tail Mutation Impairs Motor Processivity, Nature Cell Biology 12(12), 1228-1234.

[40] T.D. Pollard and W.C. Earnshaw, with J. Lippincott-Schwartz, (2008), Journal of Cell Biology Second Edition, Elsevier Inc, Philadelphia.

[41] A.J. Roberts, N. Numata, M.L. Walker, Y.S. Kato, B. Malkova, T. Kon, R. Ohkura, F. Arisaka, P.J. Knight, K. Sutoh and S.A. Burgess, (2009), AAA+ Ring and linker swing mechanism in the dynein motor. Cell 136, 485-495.

[42] J.L. Ross, K. Wallace, H. Shuman,Y.E. Goldman and E.L. Holzbaur, (2006), Processive bidirectional motion of dynein-dynactin complexes in vitro. Nat Cell Biol 8, 562-570 (2006).

[43] S.C. Schaffner, and J.V. José, (2006), Biophysical Model of Self-Organized Spindle Formation Patterns without Centrosomes and Kinetochores, PNAS 103(30), 11166-11171.

[44] M. Schliwa, and G. Woehlke, (2003), Molecular Motors, Nature 422, 759-765.

[45] M. Schuster, S. Kilaru, P. Ashwin, C. Lin, N.J. Severs, and G. Steinberg, (2011), Controlled and Stochastic Retention Concentrates Dynein at Microtubule Ends to Keep Endosomes on Track, The EMBO Journal 30, 652-664.

[46] M. Schuster, S. Kilaru, G. Fink, J. Collemare, Y. Roger, and G. Steinberg, (2011), Kinesin-3 and dynein cooperate in long-range retrograde endosome motility along a nonuniform microtubule array. Mol Biol Cell 22, 3645-3657.

[47] D.A. Smith, and R.M. Simmons, (2001), Models of Motor-Assisted Transport of Intracellular Particles, Biophysical Journal 80, 45-68.

[48] V. Soppina, A.K. Rai, A.J. Ramaiya, P. Barak, and R. Mallik, (2009), Tug of War Between Dissimilar Teams of Microtubule Motors Regulates Transport and Fission of Endosomes, PNAS 106(46), 19381-19386.

[49] D. Tsygankov, A.W.R. Serohijos, N.V. Dokholyan, and T.C. Elston, (2009), Kinetic Models for the Coordinated Stepping of Cytoplasmic Dynein, The Journal of Chemical Physics 130, 025101.

[50] R.D. Vale, (2003), The Molecular Motor Toolbox for Intracellular Transport, Cell 112, 467-480.

[51] M.N. Weedon, R. Hastings, R. Caswell, W. Xie, K. Paszkiewicz, T. Antoniadi, M. Williams, C. King, L. Greenhalgh, R. Newbury-Ecob, and S. Ellard, (2011) Exome Sequencing Identifies a DYNC1H1 Mutation in a Large Pedigree with Dominant Axonal Charcot-Marie-Tooth Disease, American Journal of Human Genetics 89(2), 308-12.

[52] M.H. Willemsen, L.E.L. Vissers, M.A.A.P. Willemsen, B.W.M. van Bon, T. Kroes, J. de Ligt, B.B. de Vries, (2012), Mutations in DYNC1H1 cause severe intellectual disability with neuronal migration defects. Journal of medical genetics, 49(3), 179183. doi:10.1136/jmedgenet-2011-100542.

[53] J. W. Wojcieszyn, R. A. Schlegel, E. Wu, and K.A. Jacobsom, (1981), Diffusion of Injected Macromolecules within the Cytoplasm of Living Cells, PNAS 78(7), 4407-4410.

[54] K.S. Zadeh, and S.B. Shah, (2010), Mathematical Modelling and Parameter Estimation of Axonal Cargo Transport, Journal of Computational Neuroscience 28, 495-507.

[55] Y. Zhang, (2008), Three Phase Model of the Processive Motor Protein Kinesin, Biophysical Chemistry 136, 19-22.

[56] Y. Zhang, (2009), A General Two-Cycle Network Model of Molecular Motors, Physica A 388, 3465-3474.